scientific reports

Check for updates

OPEN

Understanding H-aggregates crystallization induced emissive behavior: insights from theory

Huixue Li✉, Lingling Lv, Kun Yuan, Sujuan Pan & Zhifeng Li✉

We conducted a theoretical investigation into how the molecular stacking effect impacts the photophysical properties in solid phases. Our findings indicated that in the aggregated state, the out-of-plane distorted vibration and imidazole ring stretching vibration of triimidazo-[1,3,5] triazinethe are significantly suppressed, which decreased the Huang-Rhys factor and the corresponding reorganization energy of the photophysical process, as a result, this restricted intramolecular motions and dissipation pathways of excess energy in the excited state, therefore, aggregation induced enhancement emission (AIEE) was found for the title compound from dichloromethane solution to solid state. Analysis of the emission spectrum through discrete spectral lines revealed that the main peak was affected by the vibrational modes with lower frequencies, while the middle-frequency modes influenced the shoulder peak. Furthermore, the predicted intersystem crossing rate (k_{iosk}) and reverse intersystem crossing rate (k_{risc}) using Marcus theory confirmed that an electron can successfully shift from its S_1 state to the T_1 state, however, the reverse $T_1 \rightarrow S_1$ process can not come into being due to very small k_{risc} (10^{-6}–10^{-9} s^{-1}), therefore the phosphorescence can be observed. At last, we explored the influence of charge transfer process of the title compound, our theoretical data declared this process can be ignored due to its low transfer rate.

Due to their exceptional luminosity efficiency and vibrant illumination colors, organic light-emitting materials have been organic light-emitting materials have been found extensive applications in various fields, including chemical detection, biological sensing and imaging, and photovoltaic devices[1–7]. However, the currently available fluorescent materials, which possess a macrocyclic aromatic conjugation system, face a significant challenge in research and practical applications. These organic light–emitting materials tend to pack tightly in aggregates due to their planar polycyclic aromatic structure, the π–π stacking interaction between molecules in condensed state leads to the formation of detrimental excimers at the excited state, resulting in well–known the aggregation–caused quenching (ACQ) effect[5,8,9]. This ACQ effect theoretically and practically reduces the fluorescence quantum yield of the material. Fortunately, not all organic fluorescent materials exhibit the limitations of ACQ. In fact, there is an intriguing phenomenon known as aggregation-induced emission (AIE), and they have been discovered in numerous molecular systems[4,8,10–14]. AIE allows these molecules to exhibit more efficient light emission when they aggregate, in the case of these materials, their fluorescence is either absent or extremely weak when in dilute solution, nevertheless, their luminescent intensity significantly enhances when they are in a gathered or solid state. Actually, their fluorescence quantum yield increases by several orders of magnitude when in the solid state as compared to that in a solution[7]. Up to now, it has been proved that numerous planar ACQ chromophores can be transformed into AIE materials by combination of other AIE-active unit (for instance tetraphenylethene)[15,16].

The emergence of the AIE effect has successfully overcome the limitations of the traditional fluorescent molecules utilized in photoelectric devices. This effect offers a remarkable improvement in the luminescent performance of materials and enhances the detection sensitivity. Consequently, it has garnered significant attention from both the scientific community and industry, becoming a prominent area of research in chemistry and materials science. As a result, an increasing number of studies in various fields including chemistry, biology, and materials have been conducted, leveraging the advantages provided by the AIE effect[17–22]. Besides the experimental observation, a variety of theoretical investigations have also been done to elucidate the AIE mechanisms and predict new AIE materials[8,9,23–25]. The mechanism of restricting intramolecular motion (RIM)—which involves limiting both intramolecular rotation and vibration—has been widely accepted due to its strong support from experimental evidence[9,26,27].

School of Chemical Engineering and Technology, Tianshui Normal University, Tianshui 741001, Gansu, China. ✉email: li_hx2001@126.com; lizhfe2003@163.com

J-aggregation is another mechanism proposed for AIE luminescent materials[5,28], it involves the head–tail overlap of fluorophores when both the molecules aggregate with the assistance of solvents or supermolecular self-organization. During this aggregation process, the spatial arrangement of molecules can effectively diminish the strong π–π interaction between aromatic compounds and hinder the formation of excimers, resulting in enhanced fluorescence. However, it is worth noting that not every J-aggregation possesses AIE activity[9].

While it is generally accepted that H-aggregates are non-emissive materials, there are exceptions to the rule. Some H-aggregates have been found to exhibit strong fluorescence and high efficiency[29,30]. In a recent study, Cariati and colleagues[31] reported on a pure organic molecule called cyclic triimidazole, which exhibits H-aggregation. Interestingly, this molecule exhibited weak luminescence in solution but displayed robust luminescence when in a crystalline form. To investigate its emissive behavior, the research team employed time-resolved emission spectroscopy and observed both fluorescence and phosphorescence phenomena experimentally. Notably, the compound exhibited an ultralong phosphorescence lifetime of up to one second, even at room temperature in air. While the researchers attributed the luminescent phenomenon to crystallization-induced emission based on a combination of experimental and theoretical calculations, but the actions of excited processes involved all sorts of radiative and nonradiative decay, intersystem crossing (ISC) and reverse intersystem crossing (RISC) rates between ground state (S_0), first excited state (S_1) and first triplet state (T_1), still remained undiscovered, the lack of quantitative discussion was flaw in their paper.

Currently, numerous researchers have made significant contributions to theoretical modeling and approaches related to AIE. Shuai et al. developed an algorithm to be called time-dependent density matrix renormalization group at zero and finite temperature to compute the linear absorption and fluorescence spectra of molecular gathered state, this method can provide an accurate and efficient means to calculate the spectrum of molecular aggregation[32]. Using the QM/MM model, they found the concomitant relationship between the descriptors (γ, β) and phosphorescence efficiency and lifetime, it was also revealed that the organic compounds containing n/π-groups were favorable for the room–temperature phosphorescence in organic molecules with high efficiency and long–lived afterglow synchronously[33]. Presti et al. used a recently developed excited–state electrostatic embedding model to elucidate the enhanced emission in fluorenone compound, they focused on a single-molecule process only, and found it played an important role to enhance fluorescence that the electrostatic field was induced by the crystalline environment at the excited state, Moreover, they observed a substantial bathochromic shift compared with emission in dilute solution[34]. Tang et al. introduced benzoyl or benzyl to a planar chromophore to create AIE luminogens, they analyzed and depicted the operating mechanism of these new AIE luminogens, in which the structural rigidification of these fused-ring aromatic compounds were the major factor to be responsible for their AIE effect[22]. Liang and Shuai et al. proposed that resonance Raman spectroscopy (RRS) was employed to research the microscopic mechanism of AIE, owing to the RRS amplitude is proportional to frequency times the vibrational relaxation energy of mode, therefore RRS was a direct way to confirm the AIE mechanism[35]. By the computational study, Basak et al. explained the unique fluorescence property of the H-aggregated naphthalene diimide (NDI) derivative, it was found that the $S_2 \rightarrow S_0$ transition was responsible for the fluorescence when the S_1 was a dark state, obviously it violated Kasha's rule and was accountable for the unique fluorescence properties of this type of NDI molecule[29].

In this study, we aimed to deepen AIE understanding of the luminescent mechanism about cyclic triimidazole by a comprehensive theoretical investigation. Firstly, we optimized the geometries of the compound in gas phase, solution, and aggregate state using a hybrid density function. The frequencies obtained from the optimized geometries were then used to confirm the stability of the configurations, and further calculations on optical properties were conducted. To investigate the dynamic process of photophysics, including fluorescence, phosphorescence, intersystem crossing, and internal conversion, we employed the MOMAP program to carry out. We also explored the effects of temperature, crystallization packing, and Duschinsky rotation on the radiative and nonradiative decay processes. This paper will provide valuable insights for future research in this field.

Theoretical method and computational details

The fluorescence and phosphorescence radiative decay rates can be calculated using the Einstein spontaneous emission formula, which can be expressed by integrating over the whole emission spectrum:

$$k_r(T) = \int \sigma_{emi}^{FC}(\omega) d\omega \tag{1}$$

$$\sigma_{emi}(\omega) = \frac{4\omega^3}{3\hbar c^3} \sum_{v_i f_i} P_{iv_i}(T) \left| \left\langle \theta_{f,v_f} \left| \mu_{fi} \right| \theta_{i,v_i} \right\rangle \right|^2 \delta(\omega_{iv_i fv_i} - \omega) \tag{2}$$

Here $\sigma_{emi}^{FC}(\omega)$ is the emission cross section with dimensions of cm^2, c is the velocity of light, $P_{iv_i}(T)$ is the Boltzmann population of initial states, μ_{fi} is the electric transition dipole moment, θ is the vibrational wave functions, the subscript i and f refer to initial and final states, respectively, the internal conversion (IC) processes can be treated mathematically with Fermi's golden rule by the displaced harmonic oscillator model, the IC rate can be written as follows:

$$k_{IC} = \sum_{kl} k_{ic,kl} \tag{3}$$

$$k_{ic,kl} = \frac{1}{\hbar^2} R_{kl} \int_{-\infty}^{\infty} dt[e^{-i\omega_{if}t} Z_{iv}^{-1} \rho_{ic,kl}(t, T)] \tag{4}$$

R_{kl} is the nonadiabatic transition momentum containing both diagonal and nondiagonal, Z_{iv} is the partition function, and $\rho_{ic,kl}$ is the thermal vibrational correlation function in the internal conversion process, which can be obtained by the multidimensional harmonic oscillator model in MOMAP package. The rate constants for intersystem crossing processes can be calculated using classical Marcus formula as follows:

$$k_{\mathrm{ISC\ (et)}} = \frac{2\pi}{\hbar} |H_{ij}|^2 \left(\frac{1}{4\pi\lambda k_B T}\right)^{1/2} \exp\left[-\frac{(\Delta G^0 + \lambda)^2}{4\lambda k_B T}\right] \tag{5}$$

where λ is the total reorganization energy containing inner (λ_i) and outer reorganization energy (λ_s) from the solvent, ΔG^0 is the variation of the Gibbs free energy in the process, k_B is the Boltzmann constant, and T is the temperature, here it is set as 300 K. H_{ji} refers to the spin orbit coupling (SOC) and is computed by the quadratic response function method in the Dalton program[36].

Moreover, it is possible that an excited electron in the S_1 state can be transferred to neighboring molecules, possibly affecting the luminous mechanism and further affecting the fluorescence efficiency, this charge transfer rates (k_{et}) for electron or hole can be theoretically calculated based on Marcus theory, according to two state model, the generalized Mulliken–Hush (GMH) and fragment charge difference (FCD) approximations are efficient and reliable to calculate charge transfer matrix elements, which depends strongly on the donor–acceptor distance and geometry of the system, the GMH can be expressed as follows[37]:

$$H_{ij} = \frac{m_{ij}\Delta E_{ij}}{\sqrt{(\Delta\mu_{ij})^2 + 4(m_{ij})^2}} \tag{6}$$

where ΔE_{ij} is the energy gap between the initial adiabatic state and the final one, $\Delta\mu_{ij}$ is the dipole moment difference between states *i* and *j*, and m_{ij} denotes the transition dipole moment connecting the two states. The FCD method to estimate the electron transfer matrix element is very similar to GMH formula as following[38]:

$$H_{ij} = \frac{\Delta q_{12}\Delta E_{ij}}{\sqrt{(\Delta q_1 - \Delta q_2)^2 + 4\Delta q_{12}^2}} \tag{7}$$

here, Δq_1 and Δq_2 are the D–A charges difference in the adiabatic states *i* and *j*, respectively, and Δq_{12} is the corresponding off–diagonal term.

Here we ignore the photochemistry reaction owing to that no chemical reaction was observed in the experiment, therefore based on the Jablonski diagram, there are four major de–excitation routes for the first singlet excited state, the first one is the radiative decay (k_r) from the S_1 to S_0 state; the second is the internal conversion (k_{nr}) decay from the S_1 to S_0 state; the third is the intersystem crossing (k_{isc}) from the S_1 to triplet T_1 state, the last is the charge transfer (k_{et}) from the S_1 to the adjacent molecule, thus the fluorescence quantum yield can be expressed as $\eta = k_r/(k_r + k_{nr} + k_{isc} + k_{et})$, one can see the molecular light–emitting efficiency is visibly determined by the competition between the radiative decay rate (k_r) and the nonradiative decay rate (k_{nr}, k_{isc} and k_{et}), according to the above equation, suppressing the non-radiative rate and increasing the radiative rate leads to a higher fluorescence efficiency, and a large intersystem crossing rate and a small anti-intersystem crossing rate are necessary if a high phosphorescence efficiency is desired.

The geometric optimization of the title compound at S_0, S_1 and T_1 states were implemented using B3LYP/6–31(d, p) level in gas phase and solution, the polarizable continuum model (PCM) was employed to simulate the solvent effect on molecular photophysical properties in dichloromethane (DCM), the combined quantum mechanics and molecular mechanics (QM/MM) approach was used to model the stacking surrounding in crystal, the initial guessed structure came from the crystal cell experimentally, the ONIOM method was carried out the QM/MM calculation through Gaussian09 package. In ONIOM model (as shown in Fig. 1a), the centered molecule was calculated by quantum mechanical method as a high layer, the surrounding molecules were treated by molecular mechanics with UFF forces field as low layer, meanwhile the electronic embedding scheme was taken in this model. For the S_1 state, the time dependent DFT was applied at the same basis set. Harmonic vibrational frequencies were calculated at the equilibrium geometries of the S_0, T_1 and S_1. In addition, based on the electronic structure of the title compound, the Huang–Rhys factor, normal mode displacements, nonadiabatic electronic coupling between the two electronic states were implemented using MOMAP, at last the radiative and nonradiative decay rates were computed and the fluorescent quantum yield was obtained also.

Results and discussion

The geometry and normal modes analysis. Our optimized S_0 minima of the title compound is a exactly planar molecule with C_{3h} symmetry in gas phase and in DCM, however, this molecule in aggregate state seems to be not planar and its dipole moment is 0.2271 Debye, Fig. 1a shows the dihedral angles of three imidazole rings (marked as 2, 3 and 4) and triazine ring 1 are 179.0°, 178.4° and – 177.6° respectively, which means the central molecule is slightly distorted due to the interaction from the adjacent surrounding. Nevertheless, all the optimized excited states S_1 and T_1, whether in gas phase, in DCM or in cluster, become nonplanar, it is found that the triazine ring 1 at S_1 states is completely twisted, but each imidazole ring (refer to ring 2, 3 and 4) remains basically on the same plane, it should be pointed out that the title compound consisting of three imidazole rings is nonplanar. Figure 1b visually illuminates the changes of the $S_0 \rightarrow S_1$ minima in different surroundings, the

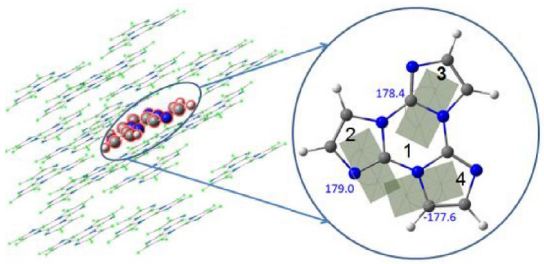

a: optimized S_0 state in cluster

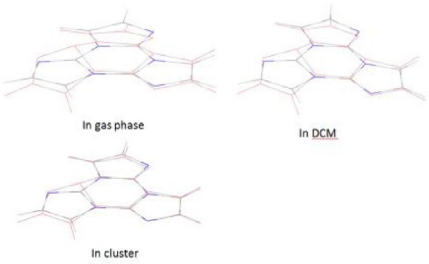

b: geometry comparison between S_0 (grey) and S_1 (red)

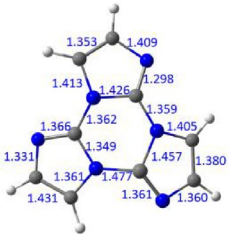

S_1 in gas phase

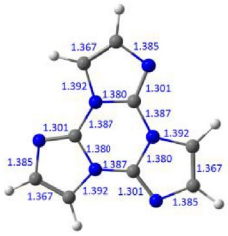

S_0 in DCM

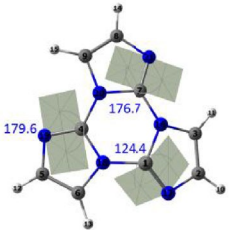

S_1 in gas phase

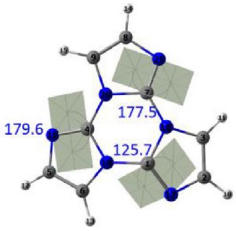

S_1 in cluster

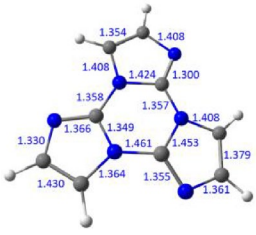

S_1 in cluster (low layer omitted)

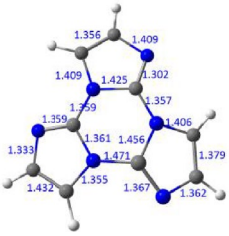

S_1 in DCM

c: Bond length of optimized S_1 and S_0 states molecule

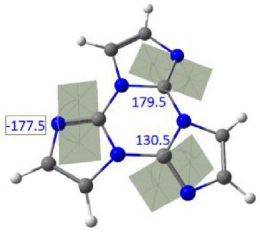

S_1 in cluster (low layer omitted)

d: the dihedral angel of S_1 states for the studied molecule

Figure 1. Bond parameters of the studied molecule in their minima by B3LYP/6–31G (d, p). ONIOM model (**a**): the centered molecule is treated by B3LYP/6–3131G**: UFF as a high layer and the surrounding molecules are fixed as a low layer, (**b**): geometry comparison between S_0 (grey) and S_1 (red), (**c**): bond length of optimized S_1 and S_0 states, (**d**): the dihedral angel of S_1 states for the studied molecule.

extent of variation for molecule-in-cluster is the smallest, and that in vacuum is the largest, though their variational tendency is the same. The three dihedral angles of the S_1 minima in gas phase, DCM and cluster are shown in Fig. 1d, in which the maximum deviations from plane are 124.4°, 125.7° and 130.5° correspond to gas phase/DCM/cluster, respectively, these data again confirm quantificationally the changing trendy in Fig. 1b. The three C–N bond in triazine ring for S_1 minima, which do not share with the imidazole rings, for the isolated molecule are 1.359, 1.362 and 1.477 Å, for the solvated molecule are 1.357, 1.359 and 1.471 Å, as for the locked molecule in cluster, those become 1.357, 1.358 and 1.461 Å (shown in Fig. 1c, the data of S_0 in vacuum and cluster attached in Supplementary Information), respectively, we can see these bond parameters in cluster have a minimum amount of change compared with these in vacuum and solution, it is clear that the intermolecular interactions constrain the deformation of the molecular geometry. In addition, it should be pointed out that the planar S_0 minima show obvious conjugative characteristic, here all the C–C and C–N bonds at the S_0 minima are actually shorter than typical single bonds, but longer than typical double bonds, for example, Fig. 1c shows all the C–C bonds are 1.367 Å and C–N bonds are between 1.301 and 1.392 Å at S_0 minimum in DCM, however, the three C–C bonds in S_1 minimum are unequal owing to broken symmetry, one shortens to 1.356 Å, while the other two lengthen to 1.379 and 1.432 Å, as for C–N bonds in S_1 state, which in three imidazole rings seem irregularity to follow, they change between 1.302 and 1.471 Å and possess typical characteristic of single bond and double band, which illustrates the π–conjugated system is completely destroyed, the electron density-difference map (Fig. 2) between the S_0 and S_1 states may explain the change, we can find the electron shift from blue area with negative value to purple area with positive value, that is, the C–N bonds corresponding to electron shifting out will be lengthened, while the C–N bonds corresponding to electron entering into will be shortened. Similarly, this situation also exists in the T_1 state in gas phase, solution and cluster, referring to Supplementary Information for details (Figs. S1 and S2).

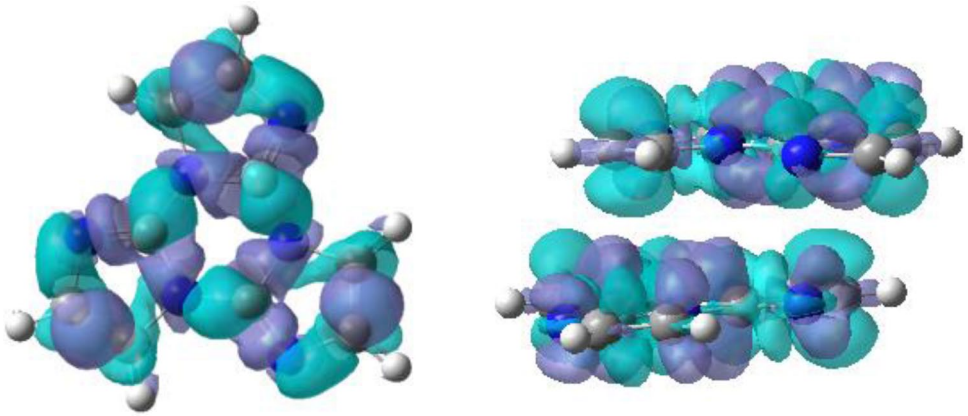

Figure 2. Electron density difference map between S_0 and S_1 in DCM (left) and in dimer (right), note the loss of electron density at the blue area and the gain in electron density at the purple area corresponding to $S_0 \rightarrow S_1$.

Furthermore, we investigated the effect of intermolecular interaction on frontier molecular orbital, the calculated energy level, energy gap between frontier molecular orbital and the corresponding distributions of the highest occupied molecular orbital (HOMO) and the lowest unoccupied molecular orbital (LUMO) are shown in Fig. 3 and Fig. S3. One can find that both the HOMO and LUMO maps in three environments have hardly change and indicate π characteristic, but the HOMO is a bonding orbital and LUMO is an anti–bonding orbital, in addition, owing to the molecular symmetry of S_0 minima, all the HOMOs and LUMOs are double degenerate. While there are significant changes in the frontier orbital energies, it can be observed that the HOMO energy levels increase successively in the gas phase (– 6.676 eV), solution (– 6.627 eV), and cluster (– 6.192 eV). It is worth noting that the LUMO energy level in DCM is lower than that in the gas phase, while in the cluster, it increases. Additionally, as for the energy gap between HOMO and LUMO, the smallest value of 5.585 eV is observed in DCM, followed by the cluster with 5.634 eV, and the maximum value of 5.666 eV in the gas phase.

Environment effect on photophysical properties, Huang–Rhys factor and reorganization energy. The photophysical properties for S_1 state of the title compound, including the vertical excitation energy, oscillator strength (*f*), main configuration and the assignment, are compiled and listed in Table 1. During the absorption process, the vertical excitation energies keep nearly constant under different conditions

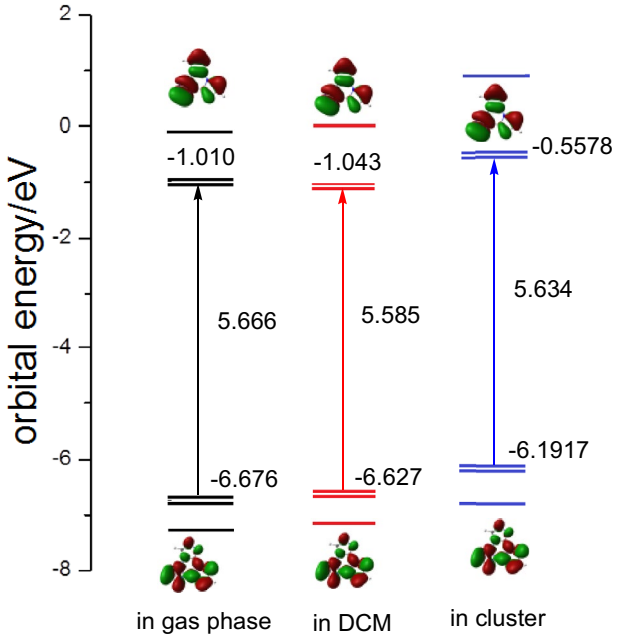

Figure 3. Energy levels diagrams of diimidazole molecule calculated based on the optimized S_0 state in gas phase, DCM and cluster, the molecular orbitals are shown together (isovalue = 0.02).

Environment	Oscillator strength	Main configuration	Assignment	λ_{cal} (nm)	λ_{exp} (nm)
The predicted absorption data of the title molecule					
In gas phase	0.1700	HOMO → LUMO	0.4111	230.1	
		HOMO−1 → LUMO + 1	0.4117		
		HOMO−2 → LUMO + 1	− 0.3086		
In DCM	0.1634	HOMO−1 → LUMO	0.4192	230.1	230
		HOMO → LUMO + 1	0.4188		
		HOMO−2 → LUMO + 1	0.3234		
In cluster	0.1493	HOMO−1 → LUMO	0.3560	232.1	
		HOMO−2 → LUMO	− 0.3405		
		HOMO → LUMO + 1	0.3351		
The predicted emission data of the title molecule					
In gas phase	0.0371	HOMO → LUMO	−0.7014	421.1	
In DCM	0.0851	HOMO → LUMO	−0.7032	405.6	390 (10^{-4} M), 400 (10^{-2} M)
In cluster	0.0386	HOMO → LUMO	0.7004	388.6	400 (crystal), 425 (powder)

Table 1. Absorption and emissions of the title compound according to TDDFT calculations, together with the experimental data. B3LYP/6–31g (d, p):uff = qeq method is employed in cluster.

(230 nm), which matches well with the experimental observations. The main transition configuration undergoes slight changes between the solution and solid state, besides HOMO−1 → LUMO and HOMO → LUMO + 1 in DCM and in cluster, for solution HOMO−2 → LUMO + 1 is one of the main transition configuration, and for cluster HOMO−2 → LUMO is main transition also, while the oscillator strength is smaller slightly in solid phase (0.1493) than that in DCM (0.1634). Our investigation of the emission process revealed that the transition configuration from HOMO to LUMO was the dominant process in both the DCM and solid phases. Nevertheless, we observed a significant decrease in oscillator strengths compared to the excitation process. Additionally, it was discovered theoretically that the maximum emission wavelength was redshifted from solid phase (388.6 nm) to DCM (405.6 nm). These theoretical predictions were in good agreement with experimental data (390 nm (10^{-4} M), 400 nm (10^{-2} M) in DCM and 400 nm in crystal, 425 nm in powder), where the maximum emission peaks were observed to be 400 nm in the crystal and 425 nm in the powder. In addition, we studied some dynamic parameters about photophysics, in which the radiative and nonradiative rates, the ISC and RISC rates, and the rate of photoinduced electron transfer were involved. It is well–known Huang–Rhys factor (HR) and reorganization energy (λ) are crucial parameters to estimate these rates with formula 2, 4 and 5[39,40], thus both the values have been obtained firstly using MOMAP package and part are shown in Table 2 (all the data are shown

	Freq. (cm^{-1})	R (cm^{-1})	λ_{reorg} (cm^{-1})	HR	FC
In cluster					
v_2	143.6	225.6	193.2	1.3452	0.0215
v_5	259.2	10.7	103.4	0.3988	0.0096
v_6	284.9	43.9	151.8	0.5327	0.0153
v_7	310.5	201.6	459.9	1.4812	0.0191
v_9	441.5	62.3	81.7	0.1851	0.0018
v_{11}	515.1	825	428	0.8309	0.0237
v_{13}	561.9	95.2	1129.8	2.0104	0.0098
v_{14}	577.9	32.8	256.9	0.4445	0.0116
v_{33}	1105.2	94.5	445.6	0.4032	0.0098
v_{38}	1221.1	27.3	556.4	0.4556	0.0121
v_{46}	1478.5	2487.5	947.9	0.641	0.0192
v_{50}	1661	31.1	1027.1	0.6183	0.0185
v_{51}	1712.3	149.5	1274.7	0.7444	0.0221
In solvent					
v_3	111.1	8.4	1622.6	14.6008	0
v_{16}	633.2	1.6	2178.1	3.4395	0.0013
v_{51}	1687	10.1	1110.3	0.6579	0.0396

Table 2. The selected reorganization energy (λ_{reorg}/cm^{-1}) by NMA method in $S_1 \rightarrow S_0$ process in cluster, frequencies of S_1 state, nonadiabatic coupling term (R), Huang–Rhys factor (HR), and Franck–Condon factors (FC).

in Tables S1, S2, S3 and S4), the associated nonadiabatic coupling term R, the corresponding normal vibrational frequencies and the Franck–Condon (FC) factors are listed together.

When considering the fluorescence process, we discovered that the total reorganization energy in the cluster (11,359 cm^{-1}, or 1.408 eV) is smaller than that in DCM (13,467 cm^{-1}, or 1.670 eV), which was consistent with the aforementioned geometrical changes. Using the normal mode analysis (NMA) method[41,42], we can conclude that in a solution environment, the vibrational modes with 1687, 633.2, and 111.1 cm^{-1} frequencies present the largest reorganization energies after analyzing the data, however, when considering the modes in a cluster, their frequencies become 1712, 1661, and 561.9 cm^{-1} respectively (see Tables S1, S3, S4 and Fig. 4). The insets in Fig. 4 visually depict that the main contribution to reorganization energies comes from low–frequency and middle–frequency modes. It is evident from the data that the λ values in DCM are generally larger than those in the cluster due to the molecular stacking effect.

Because reorganization energy is proportional to Huang–Rhys factor ($\lambda_i = h\nu HR_i$), and accordingly, the larger the λ is, usually the larger the HR is. It can be seen that the largest HR for the title compound is 2.010 in cluster, which is associated with the vibrational mode of frequency 561.9 cm^{-1}, and is assigned to the twisted vibration of triazine rings as shown in Fig. 5, both the other vibrational modes with low frequencies (143.6 and 310.5 cm^{-1}) possess the second large HR values (corresponding 1.3452 and 1.4812), they correspond to the twisted vibration of triazine rings as well, furthermore, middle–frequency vibrations (1478.5, 1661, and 1712.3 cm^{-1}) make a significant contribution to HR (0.641, 0.6183, and 0.7444) too, which are assigned to the C–C and C–N stretching vibration in triazine rings.

To probe the mechanism of the emissive behavior about the studied system, we investigated the lifetime of the excited state and fluorescence quantum yield of the title compound in DCM and cluster, the calculated k_r and k_{nr} are listed in Table 3. It can be found that: (i) taking Duschinsky rotation effect (DRE) into account, the calculated k_r of the title compound are 1.617×10^7 s^{-1} in DCM and 1.862×10^7 s^{-1} in cluster at 300 K, the corresponding fluorescence lifetime are 61.8 ns and 53.7 ns respectively, unfortunately the observed in cluster is 15.29 ns and in DCM is 7.84 ns, obviously, there remains a considerable gap between the theoretical and calculated values, but their trend of change is consistent; (ii) no matter in DCM or in cluster, the predicted k_{nr} are almost 3-orders larger than the k_r under the same conditions, if ignoring DRE, the k_r and k_{nr} decrease significantly to 10^4 s^{-1} and

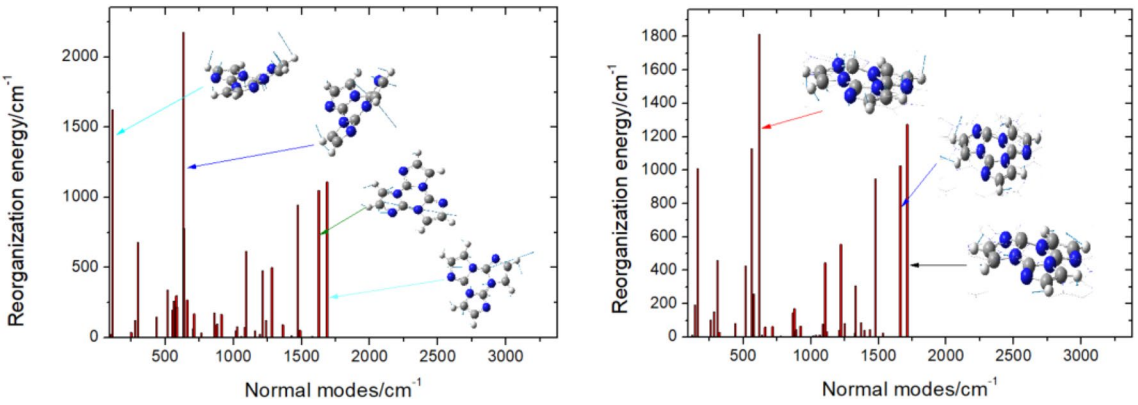

Figure 4. Calculated the reorganization energies from the normal modes in DCM and in cluster.

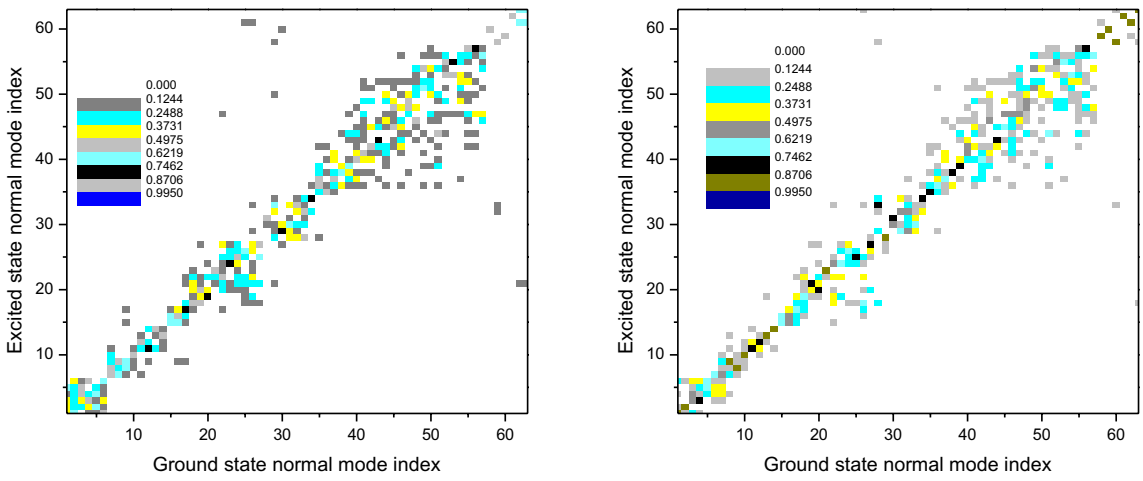

Figure 5. Duschinsky rotation matrix of triimidazole molecule corresponding to $S_1 \rightarrow S_0$ process in DCM and in cluster.

Duschinsky rotation effect (DRE)				No Duschinsky rotation effect (DRE)		
T (K)	k_r (s^{-1})	k_{nr} (s^{-1})	η	k_r (s^{-1})	k_{nr} (s^{-1})	η
In vacuum						
50	2.342×10^{7}	4.775×10^{11}		8.000×10^{3}	1.124×10^{7}	
100	2.221×10^{7}	4.457×10^{11}		1.027×10^{4}	1.255×10^{7}	
150	2.220×10^{7}	4.775×10^{11}		1.027×10^{4}	1.471×10^{7}	
200	2.152×10^{7}	3.856×10^{11}		1.250×10^{4}	1.804×10^{7}	
250	2.083×10^{7}	3.621×10^{11}		1.574×10^{4}	2.308×10^{7}	
300	2.015×10^{7}	3.425×10^{11}		2.030×10^{4}	3.064×10^{7}	
In DCM						
50	7.053×10^{7}	9.137×10^{10}		6.014×10^{3}	5.357×10^{5}	
100	7.014×10^{7}	1.084×10^{11}		6.579×10^{3}	5.938×10^{5}	
150	6.942×10^{7}	1.285×10^{11}		7.596×10^{3}	6.945×10^{5}	
200	6.856×10^{7}	1.477×10^{11}		9.177×10^{3}	8.572×10^{5}	
250	6.761×10^{7}	1.653×10^{11}		1.150×10^{4}	1.114×10^{6}	
300	1.617×10^{7}	1.811×10^{11}	8.93×10^{-3}%	1.483×10^{4}	1.514×10^{6}	0.98%
In cluster						
50	2.057×10^{7}	1.149×10^{10}		1.302×10^{7}	7.191×10^{7}	
100	2.033×10^{7}	1.337×10^{10}		1.299×10^{7}	7.437×10^{7}	
150	1.997×10^{7}	1.684×10^{10}		1.294×10^{7}	8.004×10^{7}	
200	1.955×10^{7}	2.196×10^{10}		1.288×10^{7}	8.983×10^{7}	
250	1.909×10^{7}	2.885×10^{10}		1.281×10^{7}	1.048×10^{8}	
300	1.862×10^{7}	3.765×10^{10}	0.049%	1.280×10^{7}	1.264×10^{8}	9.19%

Table 3. Calculated radiative decay rate (k_r) and nonradiative decay rate (k_{nr}) from S_1 to S_0 and the corresponding fluorescence quantum yield (η) at different temperatures for the title molecule. The calculated phosphorescence radiative rates k_p in vacuum/solution/cluster are 0.126/0.128/0.130 s^{-1} at 300 K, respectively. The experimental data of the fluorescence quantum yield is 2% in DCM, and 18% in solid state[31].

10^6 s^{-1} in DCM; (iii) when the temperature goes up from 50 to 300 K, the k_r and k_{nr} in cluster changes very little compared to the vacuum and solution conditions.

In general, the non–radiative decay process will dissipate the more excited energy when the reorganization energy in this process is larger[16], considering Duschinsky rotation and mode distortion, the twisting motion with low–frequency and the stretching motion with middle–frequency in DCM couple strongly with the electronic excitation, which dissipates the energy efficiently by a fast decay rate (5.52 ps, the inverse of k_{nr}), while the restricted molecule in cluster, these motions are impeded by the intermolecular forces with a much slower decay rate (26.6 ps). The caused mode mixing by the Duschinsky rotation is graphically shown in Fig. 5 and it can be seen the modes with low- and middle-frequency play an important role[43], we found the mixing of low-frequency mode in solution is more serious than that in cluster. In addition, because the title molecule in cluster is surrounded by adjacent molecules, the proportion of the displaced harmonic oscillator increases while that of the distorted displaced harmonic oscillator decreases, it can be inferred that the Duschinsky effect during the emission process is weakened[44,45], therefore the η value will increase theoretically, if we solely took into account the radiation decay and internal conversion without Duschinsky effect, the fluorescence quantum yield (9.19%) of the triazinethe in cluster is 9.4 times higher than that (0.98%) in DCM, when Duschinsky effect is under consideration, the η value is expected to increase 55-fold from 8.93×10^{-3}% in DCM to 0.049% in cluster. According to the above theoretical analysis, we believed that the low-frequency and middle-frequency motions in solid phase are hindered and the energy dissipation pathway by the internal conversion are slowed down, thus the AIE characteristic of the title molecule from DCM to solid phase is found.

Moreover we computed the approximate FC factors of all the normal modes to simulate the vibronic fluorescent spectrum of the title molecule in cluster. Based on the harmonic oscillator model, the FC factor can be expressed by a Poisson distribution as follows[46]:

$$\prod_k \left|\left\langle \theta_{fv_k} | \theta_{i0} \right\rangle\right|^2 = \prod_k \frac{S_k^{v_k}}{v_k!} e^{-S_k} \tag{6}$$

For both the different electronic states of a molecule in aggregate state, a small displacement in the potential energy surface can be anticipated due to the steric inhibition, and the harmonic oscillator model should be a good approximation. Here for simplicity, we only considered the contribution to the spectrum of the $0\rightarrow0$, $0\rightarrow1$ and $0\rightarrow2$ vibrational transitions, the other higher vibrational transitions were neglected, thereby the FC factor about vibrational modes will be simplified as $\frac{1}{2}S_k^3 e^{-3S_k}$, S_k is the HR factor of the kth mode, some selected modes are listed in Table 4 (other shown in Table S4), it can be found that the FC factors with low frequencies 143.6, 310.5,

	In gas phase		In DCM		In cluster	
	$S_1 \rightarrow T_1$	$T_1 \rightarrow S_1$	$S_1 \rightarrow T_1$	$T_1 \rightarrow S_1$	$S_1 \rightarrow T_1$	$T_1 \rightarrow S_1$
SOC (cm^{-1})	4.19	3.68	4.01	3.70	2.98	2.23
λ_{reorg})eV)	3.408	2.573	2.094	2.107	2.349	2.029
ΔE (eV)	−4.395	4.395	−5.413	5.413	−0.879	0.879
k_{isc} or k_{risc} (s^{-1})	3.262×10^6	2.091×10^{-8}	2.340×10^6	4.793×10^{-10}	2.041×10^5	2.912×10^{-9}

Table 4. Spin–orbital coupling (SOC)/cm^{-1}, reorganization energy (λ_{reorg})/eV between the S_1 and T_1 states using NMA and the DPES methods, adiabatic energy difference ΔE of both the S_1 and T_1 states, intersystem crossing rate (k_{isc}), and reverse intersystem crossing rate (k_{risc}) of the title compound at the S_1 and T_1 minima. The λ_{reorg} is from NMA method with internal coordinate, the temperature is 300 K, k_{isc} corresponds to $S_1 \rightarrow T_1$ and k_{risc} corresponds to $T_1 \rightarrow S_1$.

515.1 cm^{-1} are fairly large, which impact signally on the shape of the emission spectrum, we adopted Lorentzian function to fit the emission spectrum with 500 cm^{-1} full width at half maximum (FWHM), the spreading linetype of the modes with low–frequency will overlap together with the main peak (referring to $0 \rightarrow 0$ electron transition), which makes the main emission peak red shift about 345 cm^{-1}, i.e. corresponding 394 nm. The modes with 1478.5, 1661.0, and 1712.3 cm^{-1} also make a significant contribution to HR and the spectrum, it leads to the shoulder peak in emitting spectrum and the peak position is 1625 cm^{-1}, i.e., corresponding 415 nm, which exactly matches with the shape of the emitting spectrum as detected in experiment (main peak is 400 nm and shoulder peak is 420 nm). Figure 6 diagrammatized the simulated vibronic emissive spectrum and the distribution characteristics of FC factors. Additionally Fig. S4 presented the simulated emissive spectra of the studied molecule with FWHM 300 and 400 cm^{-1} as a contrast.

ISC, RISC and photo induced charge transfer rates. Experimentally, fluorescence and phosphorescence of the title molecule were detected simultaneously. As is well established, the process of phosphorescent emission is closely related to intersystem crossing, to gain insight into this photophysical mechanism, we used the classical Marcus theory to investigate the intersystem crossing rate (k_{isc}) and the reverse intersystem crossing rate (k_{risc}). Table 4 provided information on the adiabatic energy difference ΔE_{S1-T1} between the S_1 and T_1 states, as well as the reorganization energies (λ_{reorg}) and spin-orbital coupling (SOC). Here the λ_{reorg} were from NMA with internal coordinate[47], SOC were carried out using Dalton program.

It can be found that the ΔE_{S1-T1} is particularly sensitive to the environment, when the title molecule is put into DCM, the computed ΔE_{S1-T1} is − 5.413 eV, when the molecule is locked in cluster, the ΔE_{S1-T1} decreases dramatically to − 0.879 eV. In comparison, the associated λ_{reorg} in solution and crystal are not changing much, of which the $S_1 \rightarrow T_1$ process is 2.094 eV in DCM and the reverse process $T_1 \rightarrow S_1$ is 2.107 eV. In cluster, the λ_{reorg} of ISC process becomes 2.349 eV and the reverse process decreases to 2.029 eV. For details about reorganization energy using NMA method, each value vs vibrational mode is given in Table S4.

Because of lack of the relativistic effect from heavy atom in the title compound, as predicted, the SOC data are considerably small and less than 5 cm^{-1}, when temperature is set as 300 K and H_{ij} takes SOC value, the estimated k_{isc} and k_{risc} are obtained according formula 5 and compiled in Table 4. It can be found the k_{isc} is $2.340 \times 10^6/2.041 \times 10^5$ s^{-1} in DCM/cluster, for reverse process, the k_{risc} is $4.793 \times 10^{-10}/2.912 \times 10^{-9}$ s^{-1} in DCM/cluster. Compared with the radiative rate k_{isc}, we observed the k_{risc} in DCM or in cluster are very smaller, even can be completely ignored, thus it seems that the intersystem crossing process is remarkable but the reverse intersystem crossing is impossible, accordingly the delayed fluorescence from RISC process is improbable too. We

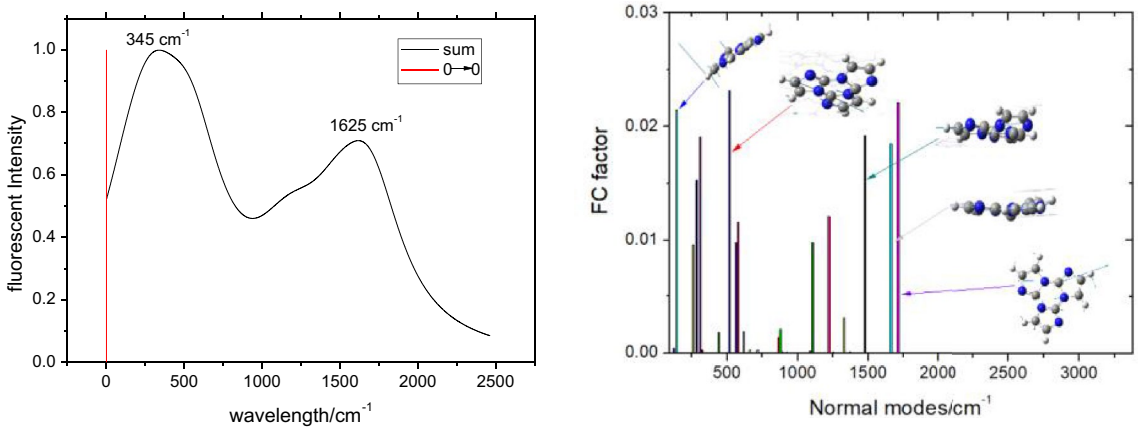

Figure 6. Simulated fluorescence spectra of triimidazole molecule using the discrete spectral line method (left) and Franck–Condon factor analysis vs normal modes (right).

have obtained the phosphorescent emission rates from the T_1 to S_0 state theoretically using the Dalton program. In DCM, the rate is 0.128 s^{-1} and in the cluster, the rate becomes 0.130 s^{-1}. These rates are higher than the k_{risc} values, suggesting that experimental observation of the phosphorescent phenomenon is likely. The corresponding lifetime of the phosphorescence in DCM/cluster was determined to be 7.81 s/7.69 s, respectively, which is similar to the measured values of 0.969 s and 0.99 s. The predicted phosphorescent emission peaks based on the vertical excited energy between the S_0 and T_1 minima are 640.8 nm in DCM (500 nm measured) and 536.8 nm in the cluster (525 nm measured). These calculated results indicated that the theoretical value in solid state was in accordance with the experimental one in the phosphorescent emission process, but one in DCM is far from the observed value, which could be attributed to polarization continuum model, this model may not fully capture the intricate interactions between the solute and solvent molecules, leading to inaccuracies in the calculated spectra. In addition, the choice of the exchange–correlation functional within DFT can affect the accuracy of the calculations, certain functionals may not properly account for the effects of excited-state and solvent–solute interactions, leading to deviations from experimental results (Table 5).

In the S_1 state of the title compound, the excited electron has the possibility of transferring to adjacent molecules—so called photo-induced intermolecular electron-transfer[48–50], there are two paths for electron transfer at random and shown in Fig. 7 (path 1 and path 2 for short). With the aid of the crystal structure, we can find the inter-centroids separation is 3.73 Å for the dimer of path 1 and 3.95 Å for path 2, but the perpendicular distance between both the molecular planes for path 1 is 3.29 and path 2 is 3.20 Å. When an excited electron in the donor goes to a neighboring molecule, the excited molecule will quickly relax to the ground state with a positive charge, meanwhile the acceptor with a negative charge will reorganize to its lowest energy state too, thus the reorganization energy includes two parts, which are associated with change of molecular geometries above mentioned, according to ONIOM model, the λ_{reorg} is 1.05 eV by the displacement of potential energy surface method in this case. When involved both dimers were taken out from its unit cell, only wavefunction and energy consistence were done and no geometrical optimization performed, the electronic coupling strength (H_{ab} instead of H_{ij} to distinguish) can be calculated using GMH and FCD approximations by ωB97X/6–31G(d,p), the H_{ab} of path 1 is 0.157 eV with an open source software[51], however, the H_{ab} of path 2 decreases to 0.072 eV. Here it is important to emphasize we can observe that the electron density and its difference are both distributed on both molecules simultaneously from the dimer in Fig. 2, this suggests that due to the presence of strong intermolecular interactions, the characteristics of electron transfer seem less pronounced when the molecule transitions from the ground state to the excited state. At the same time, we calculated the hole-electron Coulomb attractive energy (exciton binding energy) in dimer which is 4.12 eV by Multiwfn program[52], this estimated value indicates that charge transfer in the dimer is not easy[29].

From a quantum mechanics perspective, H_{ab} is proportional to the orbital overlap of the wave function between the donor and acceptor during the electron transfer process. By examining the molecular configuration overlap in the dimer of path 1 and path 2 in Fig. 6, it can be concluded that the overlap between the monomers in path 1 is greater, resulting in a larger H_{ab} than path 2. Nevertheless, the plane spacing between both the molecular planes for the path 1 is larger than one of the path 2, which will decrease the electron transfer rates, as the energy difference ΔE of the donor and acceptor instead of the driving force, the photo–induced electron transfer rates k_{et} for path 1 is 1.42×10^5 s^{-1} according to Marcus theory, while the k_{et} for path 2 is 1.68×10^5 s^{-1}.

Up to now, we have obtained the radiation decay rate (k_r), internal conversion rate (k_{nr}), and intersystem crossing rate (k_{isc}) of the title compound in DCM and in cluster, in addition, the electron transfer rate (k_{et}) in cluster was gained as well. According to the formula $\eta = k_r/(k_r + k_{nr} + k_{isc} + k_{et})$, the simulated fluorescence quantum yield

	Distance (Å)	λ_{reorg} (eV)	GMH (eV)	ΔE (eV)	k_{et} (s^{-1})	FCD (eV)	ΔE (eV)	k_{et} (s^{-1})
Electron transfer (ωB97X/6–31G (d,p))								
Path 1	3.72	1.05	0.157	0.315	1.42×10^5	0.157	0.315	1.42×10^5
Path 2	3.96	1.05	0.072	0.144	1.68×10^5	0.072	0.144	1.68×10^5

Table 5. Distance of dimer, λ_{reorg} and charge transfer coupling with GMH and FCD approximations corresponding to excited charge transfer process, and charge transfer rate (k_{et}).

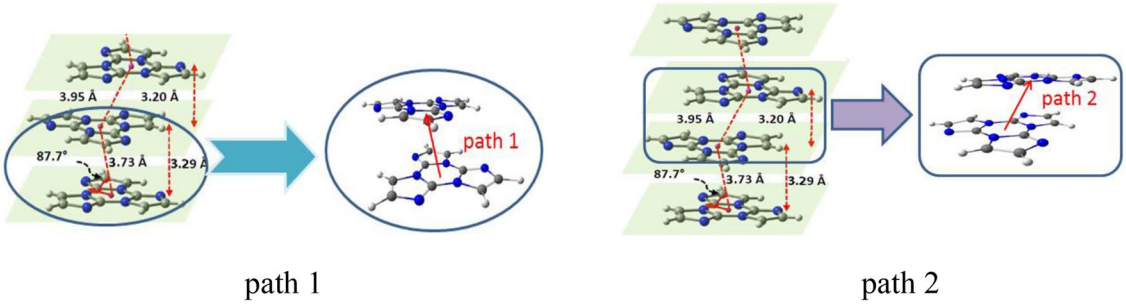

Figure 7. The intermolecular distances for path 1 and path 2 in dimers.

of this material is 8.93×10^{-3}% in DCM, and 0.049% in cluster under the DRE, when the DRE was ignored, the η increases to 0.98% in DCM (here no electron transfer) and 9.19% in cluster with the effect of electron transfer, here the calculated k_{nr} is extremely large compared with the other rates, which determines the simulated η of the material decisively, it has been discovered that the fluorescence quantum yield is not significantly affected by the absence of electron transfer and intersystem crossing.

Conclusion

In summary, employing QM/MM method and Marcus theory, we explored theoretically the photophysical and charge transfer properties of cyclic triimidazole ($C_9H_6N_6$). Results showed that, deformation of out–plane of triazine ring and imidazole motions are responsible for the photophysical properties, and triazine ring's deformation and imidazole motions are effectively suppressed in solid phase. Therefore, HR factors and reorganization energies are smaller in aggregate state in comparison with those in DCM, and energy consumption pathways for the internal conversion from excited state to ground state are hindered, this brings the AIE characteristic of the title compound, the calculated fluorescence quantum yield η is 0.98% in DCM and 9.19% in cluster without DRE respectively. The simulated emission spectrum by discrete spectral lines indicated the main peak is affected by the lower-frequency modes and shoulder peak of the emission spectrum is affected by the modes with middle frequency. Furthermore, the predicted k_{isc} and k_{risc} about ISC and RISC process using Marcus theory confirm that the electron can successfully shift from the S_1 to T_1 state, however, the reverse $T_1 \rightarrow S_1$ process cannot come into being duo to very small k_{risc} (10^{-6}–10^{-9} s^{-1}), so the phosphorescence can be observed. At last, we explored the mechanism about the electron transfer from the excited state S_1 to the adjacent molecule, our theoretical data declared this process can be ignored due to its low electron transfer rate.

Data availability

The data that support the findings of this study are available from the corresponding author upon reasonable request.

Received: 7 April 2023; Accepted: 27 July 2023
Published online: 31 July 2023

References

1. Li, M. *et al.* Phase regulation and defect passivation enabled by phosphoryl chloride molecules for efficient quasi-2d perovskite light-emitting diodes. *Nano-Micro Lett.* **15**(08), 188–198 (2023).
2. Park, J., Lim, J. & Lee, J. Y. A silane-based host material with improved electron transport properties for phosphorescent OLEDs with high efficiency and low efficiency roll-off. *Sci. China Mater.* **66**, 1997–2003 (2023).
3. Zheng, Y. *et al.* Remarkable mechanochromism and force-induced thermally activated delayed fluorescence enhancement from white-light-emitting organic luminogens with aggregation-induced emission. *Chin. Chem. Lett.* **33**(10), 4536–4540 (2022).
4. Jin, G. *et al.* Multifunctional organic nanoparticles with aggregation-induced emission (AIE) characteristics for targeted photodynamic therapy and RNA interference therapy. *Chem. Commun.* **52**, 2752–2755 (2016).
5. Mei, J., Leung, N. L., Kwok, R. T., Lam, J. W. & Tang, B. Z. Aggregation-induced emission: Together we shine, united we soar!. *Chem. Rev.* **115**, 11718–11940 (2015).
6. Ha, J., Lim, J. & Lee, J. Y. A novel benzo[4,5]furo[3,2-d]pyrimidine-based host as a n-type host for blue phosphorescent organic light-emitting diodes. *Sci. China Mater.* **65**(04), 1028–1033 (2022).
7. Nirmalananthan, N. *et al.* Crystallization and aggregation-induced emission in a series of pyrrolidinylvinylquinoxaline derivatives. *J. Phys. Chem. C* **122**, 11119–11127 (2018).
8. Hang, L., Shen, C., Shen, B. & Yuan, H. Insight into the in vivo fate of intravenous herpetrione amorphous nanosuspensions by aggregation-caused quenching probes. *Chin. Chem. Lett.* **33**(11), 4948–4951 (2022).
9. Mei, J. *et al.* Aggregation-induced emission: The whole is more brilliant than the parts. *Adv. Mater.* **26**, 5429–5479 (2014).
10. Luo, L. J. *et al.* Aggregation-induced emission of 1-methyl-1,2,3,4,5-pentaphenylsilole. *Chem. Commun.* **18**, 1740–1741 (2001).
11. Chen, P. *et al.* Enantioselective recognition based on aggregation-induced emission. *Chin. Chem. Lett.* **34**(06), 100–110 (2023).
12. Pathak, S. K. *et al.* Aromatic π–π driven supergelation, aggregation induced emission and columnar self-assembly of star-shaped 1,2,4-oxadiazole derivatives. *J. Mater. Chem. C* **4**, 6546–6561 (2016).
13. Zhao, R. *et al.* Designing anticancer combretastatin A-4 analogues with aggregation-induced emission characteristics. *Sci. China Chem.* **65**(04), 694–698 (2022).
14. Fei, Z., Zhao, C., Gang, L., Fan, C. & Pu, S. Tetraphenylethene-based highly emissive fluorescent molecules with aggregation-induced emission (AIE) and various mechanofluorochromic characteristics. *Tetrahedron Lett.* **59**, 836–840 (2018).
15. Wang, Y. *et al.* Introductory lecture: Recent research progress on aggregation-induced emission. *Faraday Discuss.* **196**, 9–30 (2017).
16. La, D. D., Bhosale, S. V., Jones, L. A. & Bhosale, S. V. Tetraphenylethylene-based aie-active probes for sensing applications. *ACS Appl. Mater. Interfaces* **10**, 12189–12216 (2018).
17. Zeng, L. *et al.* AIE molecules uv-filtering effect improves the photostability of organic solar cells. *Adv. Opt. Mater.* **10**, 2200968 (2022).
18. Yun, Z., He, S., Yang, J., Hao, S. & Ni, Z. Study on TICT emission of TPE-BODIPY derivatives mediated by methyl group on BODIPY. *Opt. Mater.* **81**, 102–108 (2018).
19. Qin, W. *et al.* Ultrabright red AIEgens for two-photon vascular imaging with high resolution and deep penetration. *Chem. Sci.* **9**, 2705–2710 (2018).
20. Gu, X. *et al.* Corannulene-incorporated aie nanodots with highly suppressed nonradiative decay for boosted cancer phototheranostics in vivo. *Adv. Mater.* **30**, 1801065 (2018).
21. Wang, Z. *et al.* Seeing the unseen: AIE luminogens for super-resolution imaging. *Coord. Chem. Rev.* **451**, 214279 (2022).
22. Zhang, Y. *et al.* Aggregation-induced emission and the working mechanism of 1-benzoyl and 1-benzyl pyrene derivatives. *Phys. Chem. Chem. Phys.* **20**, 9922–9929 (2018).
23. Liang, Y. *et al.* Theoretical study of the thermally activated delayed fluorescence (TADF) combined with aggregation-induced emission (AIE) molecular solid-state effect on the luminescence mechanism. *Chem. Phys. Lett.* **811**, 140257 (2023).
24. Wang, B., Wang, X., Wang, W. & Liu, F. Exploring the mechanism of fluorescence quenching and aggregation-induced emission of a phenylethylene derivative by QM (CASSCF and TDDFT) and ONIOM(QM:MM) calculations. *J. Phys. Chem. C* **120**, 21850–21857 (2016).

25. Qian, H. *et al.* Suppression of Kasha's rule as a mechanism for fluorescent molecular rotors and aggregation-induced emission. *Nat. Chem.* **9**, 83–87 (2016).
26. Leung, N. L. C. *et al.* Restriction of intramolecular motions: The general mechanism behind aggregation-induced emission. *Chemistry* **20**, 15349–15353 (2015).
27. Meher, N., Panda, S., Kumar, S. & Iyer, P. K. Aldehyde group driven aggregation-induced enhanced emission in naphthalimides and its application for ultradetection of hydrazine on multiple platforms. *Chem. Sci.* **9**, 3978–3985 (2018).
28. Zhao, Z., Lam, J. W. Y. & Tang, B. Z. Self-assembly of organic luminophores with gelation-enhanced emission characteristics. *Soft Matter* **9**, 4564–4579 (2013).
29. Basak, S., Nandi, N., Bhattacharyya, K., Datta, A. & Banerjee, A. Fluorescence from an H-aggregated naphthalenediimide based peptide: Photophysical and computational investigation of this rare phenomenon. *Phys. Chem. Chem. Phys.* **17**, 30398–30403 (2015).
30. Bayda, M. *et al.* Fluorescent H-aggregates of an asymmetrically substituted mono-amino Zn(II) phthalocyanine. *Dalton Trans.* **46**, 1914–1926 (2017).
31. Lucenti, E. *et al.* H-aggregates granting crystallization-induced emissive behavior and ultralong phosphorescence from a pure organic molecule. *J. Phys. Chem. Lett.* **8**, 1894–1898 (2017).
32. Ren, J., Shuai, Z. & Chan, G.K.-L. Time-dependent density matrix renormalization group algorithms for nearly exact absorption and fluorescence spectra of molecular aggregates at both zero and finite temperature. *J. Chem. Theory Comput.* **14**, 5027–5039 (2018).
33. Ma, H., Peng, Q., An, Z., Huang, W. & Shuai, Z. Efficient and long-lived room-temperature organic phosphorescence: Theoretical descriptors for molecular designs. *J. Am. Chem. Soc.* **141**, 1010–1015 (2019).
34. Presti, D. *et al.* Understanding aggregation-induced emission in molecular crystals: Insights from theory. *J. Phys. Chem. C* **121**, 5747–5752 (2017).
35. Zhang, T. *et al.* Spectroscopic signature of the aggregation-induced emission phenomena caused by restricted nonradiative decay: A theoretical proposal. *J. Phys. Chem. C* **119**, 5040–5047 (2015).
36. Dalton, a molecular electronic structure program, Release Dalton2013 (2013). http://daltonprogram.org.
37. Cave, R. J. & Newton, M. D. Generalization of the Mulliken–Hush treatment for the calculation of electron transfer matrix elements. *Chem. Phys. Lett.* **249**, 15–19 (1996).
38. Voityuk, A. A. & Rösch, N. Fragment charge difference method for estimating donor–acceptor electronic coupling: Application to DNA π-stacks. *J. Chem. Phys.* **117**, 5607–5616 (2002).
39. Fan, J., Lin, L. & Wang, C.-K. Molecular stacking effect on photoluminescence quantum yield and charge mobility of organic semiconductors. *Phys. Chem. Chem. Phys.* **19**, 30147–30156 (2017).
40. Niu, Y. *et al.* MOlecular MAterials Property Prediction Package (MOMAP) 1.0: A software package for predicting the luminescent properties and mobility of organic functional materials. *Mol. Phys.* **116**, 1078–1090 (2018).
41. Li, H. *et al.* A study on photo-induced intramolecular electron-transfer in fullerene-benzothiadiazole-triphenylamine using time-dependent density functional theory. *Org. Electron.* **14**, 105–114 (2013).
42. Jing, Y., Zheng, R., Li, H.-X. & Shi, Q. Theoretical study of the electronic–vibrational coupling in theqystates of the photosynthetic reaction center in purple bacteria. *J. Phys. Chem. B* **116**, 1164–1171 (2012).
43. Niu, Y., Peng, Q., Deng, C., Gao, X. & Shuai, Z. Theory of excited state decays and optical spectra: Application to polyatomic molecules. *J. Phys. Chem. A* **114**, 7817–7831 (2010).
44. Yan, P. *et al.* Multireference configuration interaction study on the ground and excited electronic states of the AlO+ molecule. *Comput. Theor. Chem.* **1117**, 258–265 (2017).
45. Vacher, M., Bearpark, M. J. & Robb, M. A. Direct methods for non-adiabatic dynamics: Connecting the single-set variational multi-configuration Gaussian (vMCG) and Ehrenfest perspectives. *Theor. Chem. Acc.* **135**, 187 (2016).
46. Wang, X. F., Zuo, G. F., Li, Z. F. & Li, H. X. Theoretical study of the phosphorescence spectrum of tris(2-phenylpyridine)iridium using the displaced harmonic oscillator model. *Acta Phys. Chim. Sinica.* **31**, 1667–1676 (2015).
47. Wu, Q., Peng, Q., Niu, Y., Gao, X. & Shuai, Z. Theoretical insights into the aggregation-induced emission by hydrogen bonding: A QM/MM study. *J. Phys. Chem. A* **116**, 3881–3888 (2012).
48. Zhang, W. *et al.* Physics, Photo-induced intermolecular electron transfer-effect of acceptor molecular structures. *Chin. J. Chem. Phys.* **31**, 772–778 (2018).
49. Chen, J. & Peng, Y. Photophysical properties and photo-induced intermolecular electron transfer of a novel aryl benzyl ester dendritic axially substituted silicon (iv) phthalocyanine. *Optics Health Care Biomed. Opt. VI* **11**, 18 (2014).
50. El-Nahass, M. N., Fayed, T. A. & El-Morsi, M. A. Photo-induced intermolecular electron transfer from donating amines to accepting diarylethylenes in different solvents. *J. Solution Chem.* **44**, 1757–1776 (2015).
51. Cabeza de Vaca, I., Acebes, S. & Guallar, V. Ecoupling server: A tool to compute and analyze electronic couplings. *J. Comput. Chem.* **37**, 1740–1745 (2016).
52. Lu, T. *Molclus Program, Version 1.9.9.9*, http://www.keinsci.com/research/molclus.html. Accessed 9 Sep 2022.
53. Buck, D. M. & Kunz, D. Triazine annelated nhc featuring unprecedented coordination versatility. *Organometallics* **34**, 5335–5340 (2015).

Acknowledgements

This work was supported by the Natural Science Foundation of China (No. 22063009, 22163008), the Natural Science Foundation of Gansu Province (21JR11RE035, 21JR11RE028, 21JR11RE039, 20JR5RA496, 22JR11RE192), Gansu Province Higher Education Innovation Fund Project (2021B-188, 2021B-204, 2022B-166), Innovation Fund Project for University Teachers of Gansu Province (2023A-111), Tianshui Natural Science Foundation (CXJ2022-17). Thanks to the Key Laboratory of new Molecular Materials Design and Function of Gansu Province, Theory and Computation Fuxi Innovation Team Project (0309-20210101204), Gansu Longyuan Talent Key Project (2022-77) and the Key Subject of Theoretical Calculation in Tianshui Normal University. Furthermore, we would like to thank the Cambridge Crystallographic Database for providing crystallographic data (CCDC Nos. 804409–804411)[53].

Author contributions

H.L. conceived the study and, together with Z.L., K.Y., and L.L. developed the computed method. K.Y. and H.L. did the literature search, selected the studies. Z.L. and L.L. extracted the relevant information. H.L. wrote the first draft of the paper. K.Y., L.L., and Z.L. critically revised successive draft of the paper. All authors approved the final draft of the manuscript. H.L. is the guarantor of the study.

Competing interests
The authors declare no competing interests.

Additional information
Supplementary Information The online version contains supplementary material available at https://doi.org/10.1038/s41598-023-39605-5.

Correspondence and requests for materials should be addressed to H.L. or Z.L.

Reprints and permissions information is available at www.nature.com/reprints.

Publisher's note Springer Nature remains neutral with regard to jurisdictional claims in published maps and institutional affiliations.